






## Nature of excitons in the Ti $L$ and O $K$ edges of x-ray absorption spectra in bulk SrTiO<sub>3</sub> from a combined first principles and many-body theory approach

Vijaya Begum-Hudde <sup>\*</sup>, Tobias Lojewski, Nico Rothenbach, Benedikt Eggert , Andrea Eschenlohr , Katharina Ollefs, Markus E. Gruner , and Rossitza Pentcheva <sup>†</sup>

Department of Physics and Center for Nanointegration Duisburg-Essen (CENIDE), University of Duisburg-Essen, Lotharstrasse 1, 47057 Duisburg, Germany



(Received 17 August 2022; accepted 7 February 2023; published 23 March 2023)

Based on density functional theory calculations, we model the x-ray absorption spectra of the O  $K$  edge and the Ti  $L_{2,3}$  edge in bulk SrTiO<sub>3</sub>. Taking into account excitonic effects by solving the Bethe-Salpeter equation is found to be pivotal for obtaining concurrence with the experimental data with respect to the energetic positions and relative intensity of the peaks. Moreover, analysis of the underlying interband transitions in reciprocal space reveals the origin of the prominent peaks and features in the spectra, and provides a deeper understanding of the electronic structure. For example, the characteristic four-peak structure of the Ti  $L_{2,3}$  edge results from transitions from Ti  $2p_{3/2}$  states to the unoccupied Ti  $3d t_{2g}$  (456.1 eV) and Ti  $3d e_g$  states (458.2 eV), followed by transitions from Ti  $2p_{1/2}$  states to Ti  $3d t_{2g}$  (461.8 eV) and Ti  $3d e_g$  states (463.7 eV). The first bound exciton is strongly localized in real space, and is confined to essentially one unit cell with  $3d_{xz}$  character near the Ti sites. On the other hand, the first bound exciton of the O  $K$  edge is identified as a charge-transfer type with a dominant contribution from the Ti  $3d_{xy}$  states hybridized with O  $p$  states. Moreover, the spatial distribution of the exciton wave function shows an intriguing two-dimensional spread in the  $x$ - $y$  plane, despite the three-dimensional nature of the material.

DOI: [10.1103/PhysRevResearch.5.013199](https://doi.org/10.1103/PhysRevResearch.5.013199)

X-ray absorption spectroscopy (XAS) is a well-established technique that provides information regarding the electronic, structural, and magnetic properties of technologically relevant materials. Moreover, as the energy of an absorption edge corresponds to the characteristic core-level energy of each element, XAS is an element-specific technique. In this work, we focus on the O  $K$  edge and the Ti  $L_{2,3}$  edge XAS of the paradigmatic oxide, SrTiO<sub>3</sub>, which is of significant interest due to its wide range of applications and emergent physics observed both in bulk and in heterostructures [1–4]. The Ti  $L_{2,3}$  edge and the O  $K$  edge XAS in bulk SrTiO<sub>3</sub> have been studied extensively both theoretically and experimentally. Several previous studies have reported measurements of the Ti  $L_{2,3}$  edge [5–9] and the O  $K$  edge [10]. With high brilliance synchrotron radiation and high-resolution monochromators available since the 1990s, the fine structure of SrTiO<sub>3</sub> can be measured without extrinsic broadening [7]. Applications of XAS on SrTiO<sub>3</sub> range from investigation of the pristine material to defects states [10], the electronic reconstruction at interfaces, e.g., with LaAlO<sub>3</sub> [11], the induced ferromagnetism in Fe-implanted SrTiO<sub>3</sub> [12], among others.

The bulk SrTiO<sub>3</sub> Ti  $L_{2,3}$  edge XAS spectrum exhibits four peaks resulting from the twofold split  $2p$  core level ( $L_3$  and  $L_2$

lines) due to spin-orbit coupling and in addition the twofold splitting of the  $3d$  level by the octahedral ligand field into  $t_{2g}$  and  $e_g$  manifolds. This four-peak structure is commonly observed also in other tetravalent Ti compounds with octahedral coordination, for example TiO<sub>2</sub> [13]. On the other hand, the O  $K$  edge XAS spectrum contains four prominent peaks, the first three being attributed to transitions to Ti  $t_{2g}$  and  $e_g$  [14–16] and Sr  $4d$  states [17], respectively.

On the theoretical side, a multichannel multiple scattering approach was used by Kruger *et al.* [18] to calculate the Ti  $L_{2,3}$  edge. Employing atomic multiplet theory with inclusion of the cubic crystal field, de Groot and coauthors [7] obtained Ti  $L_{2,3}$  edges consistent with experiment with respect to the energetic positions and to a large extent the relative intensities of the peaks. For a more recent review on multiplet XAS modeling techniques, see Ref. [19]. Additionally, inclusion of charge transfer in the *ab initio* configuration interaction (CI) approach yields Ti  $L_2$  edge in SrTiO<sub>3</sub> [20] concurrent with experiment with respect to the relative peak intensities and broadening including the prepeak feature. Laskowski and Blaha [21] obtained a very good agreement with experiment regarding the peak positions and relative intensities of the Ti  $L_{2,3}$  edge taking into account the electron- (core) hole interaction by solving the Bethe-Salpeter equation (BSE). According to their analysis, the splitting of each edge into two peaks was attributed to differences in the excitonic binding energies rather than the crystal-field splitting. In addition, Vinson *et al.* [22] calculated the Ti  $L_{2,3}$  edge XAS with a hybrid GW/BSE approach based on plane-wave pseudopotential wave functions using an additional term (calculated from a many-pole GW self-energy model) to the imaginary part of the self-energy to

<sup>\*</sup>Corresponding author: vijaya.begum@uni-due.de

<sup>†</sup>Corresponding author: rossitza.pentcheva@uni-due.de

reproduce the different core-hole lifetimes of the  $L_2$  and  $L_3$  edges. Recently, Woicik *et al.* [23] combined first-principles and BSE calculations with the cumulant representation of the core-hole Green's function within real-time time-dependent density functional theory to address the multielectron charge-transfer effects in XAS, and they obtained a good agreement mainly concerning the relative positions of the peaks. Furthermore, BSE calculations of the O  $K$  edge XAS by Liang *et al.* [15] rendered a better agreement with experiment compared to a  $\delta$ -self-consistent-field approach, which considers single-particle transitions.

While SrTiO<sub>3</sub> has an empty  $3d$  band, we mention here briefly previous results on the modeling of XAS for other transition-metal oxides using BSE: recent work of Duarte-Ruiz and Cocchi [24] suggested a subordinate role of excitonic effects in the Co  $K$  and  $L_{2,3}$  edges, and the O  $K$  edge XAS in LiCoO<sub>2</sub> and CoO<sub>2</sub>. On the other hand, the Mn  $L_{2,3}$  edge [21] in MnO calculated with BSE reproduced well the experimental features but with underestimated peak intensities. Employing the CI approach rendered the  $L_{2,3}$  edges in MnO and NiO [20] in very good correspondence with experiment. Recently, an *ab initio* approach combining a local multiplet model and a nonlinear cumulant approximation for the core Green's function [25] to calculate the  $2p$  x-ray photoemission spectrum of  $\alpha$ -Fe<sub>2</sub>O<sub>3</sub> and MnO rendered spectra in very good agreement with experiment.

The theoretical approaches so far have assigned the peaks of the Ti  $L_{2,3}$  edge XAS and the satellite features predominantly based on the crystal-field symmetries and the projected density of states. The aim of this work is not only to assess the role of excitonic effects on the O  $K$  and Ti  $L_{2,3}$  edge spectra by solving the BSE, but mainly to present an in-depth analysis of the prominent features of the spectra in reciprocal space in order to clearly identify the leading transitions to the unoccupied states responsible for these features. Furthermore, a central aspect of this work is to unravel the excitonic contributions by analyzing the real and reciprocal space distribution of the electronic part of the excitonic wave function, which provides crucial insight to exploit the unique features of the excitons for future applications.

The paper is structured as follows: The details of the theoretical calculations are presented in Sec. I, followed by a description of the experimental procedure in Sec. II. The electronic properties of SrTiO<sub>3</sub> including the orbital-resolved ionic contributions projected on the band structure are featured in Sec. III. In Sec. IV, we present the XAS spectra of the  $L_{2,3}$  and O  $K$  edge, compare them to experiment, and identify the underlying transitions in reciprocal space for the prominent peaks. Additional insight into the nature of excitons is provided by the real-space distribution of excitonic wave function. Finally, the results are summarized in Sec. V.

## I. COMPUTATIONAL DETAILS

The ground-state calculations were performed with the all-electron EXCITING code [26], employing PBESOL [27,28] as the starting exchange-correlation functional. A  $\Gamma$ -centered  $11 \times 11 \times 11$   $k$ -point mesh was used for the ground-state calculations with a total of 192 unoccupied bands. Muffin-tin

radii of 1.16, 1.06, and 0.767 Å for Sr, Ti, and O, respectively, are chosen with a basis-set cutoff  $R_{\text{MT}}|\mathbf{G} + \mathbf{k}|_{\text{max}} = 8.0$ . The lattice constant is set to the PBESOL value of 3.896 Å obtained with the Vienna *ab initio* simulation package (VASP) from Ref. [29]. For the XAS spectra, the electron- (core) hole interactions are accounted for by solving the Bethe Salpeter equation [30] adopting the Tamm-Dancoff approximation [31]. For the BSE calculation, an originally  $\Gamma$ -centered  $9 \times 9 \times 9$   $k$ -point mesh for the O  $K$  edge, and a  $7 \times 7 \times 7$   $k$ -point mesh for the Ti  $L_{2,3}$  edge was employed, shifted by (0.097, 0.273, 0.493). The energy threshold to include the local-field effects,  $|\mathbf{G} + \mathbf{q}|_{\text{max}}$ , is set to 3.5 a.u.<sup>-1</sup> for the O  $K$  edge, and 8.0 a.u.<sup>-1</sup> for the Ti  $L_{2,3}$  edge. A total of 20 and 10 unoccupied bands were taken into account for the O  $K$  and Ti  $L_{2,3}$  edge XAS, respectively. A Lorentzian broadening with a width of 0.35 eV for the O  $K$  edge, and 0.10–0.20 eV for the Ti  $L_{2,3}$  edge is applied to mimic the excitation lifetime.

In the current implementation of the BSE formalism, only the static screening is considered. Moreover, the Tamm-Dancoff-approximation neglects the coupling between the resonant and antiresonant components of the BSE Hamiltonian in order to reduce the calculational effort. Additional effects such as vibrational broadening [32], self-energy shifts and damping effects [22,33], which have been observed to have notable influence on the broadening and intensities of the peaks, especially on the Ti  $L_{2,3}$  edge, are neglected in the current approach.

## II. EXPERIMENTAL DETAILS

The XAS measurements were performed on commercially available SrTiO<sub>3</sub>(001) single crystals with a polished surface (Crystal GmbH) with the VEK MAG end station [34] at the PM2 beamline of the BESSY II synchrotron light source, operated by Helmholtz Zentrum Berlin. Reflection geometry, with an angle of incidence of 20° grazing, was employed to acquire the total electron yield. The absorption spectra at the oxygen  $K$  edge and the Ti  $L_{2,3}$  edges were first scaled to a monitor signal for the incident x-ray intensity (mirror current) and subsequently a linear background was subtracted before the spectra were normalized with respect to the edge-jump. To directly compare these experimental spectra to the theoretical calculations shown in the following sections, we further removed the so-called edge jump, i.e., absorption into continuum states, by subtraction of a broadened step function at 458 and 463.5 eV for the Ti  $L_{2,3}$  edges and 556.2 eV for the O  $K$  edge.

## III. ORBITAL PROJECTION OF THE IONIC CONTRIBUTIONS ON THE BAND STRUCTURE

In this section we discuss the ground-state electronic properties of SrTiO<sub>3</sub>, and present in Fig. 1 the band structure, obtained with VASP, which also shows the orbital-resolved contributions of Sr, Ti, and O indicated by circles whose size scales with the respective magnitude. The five lowest conduction bands (CBs) (up to 8 eV) are dominated by the Ti  $3d$  states [Fig. 1(c)] with the lowest three of  $t_{2g}$  character, followed by the two  $e_g$  bands. Above 14 eV we observe mixed

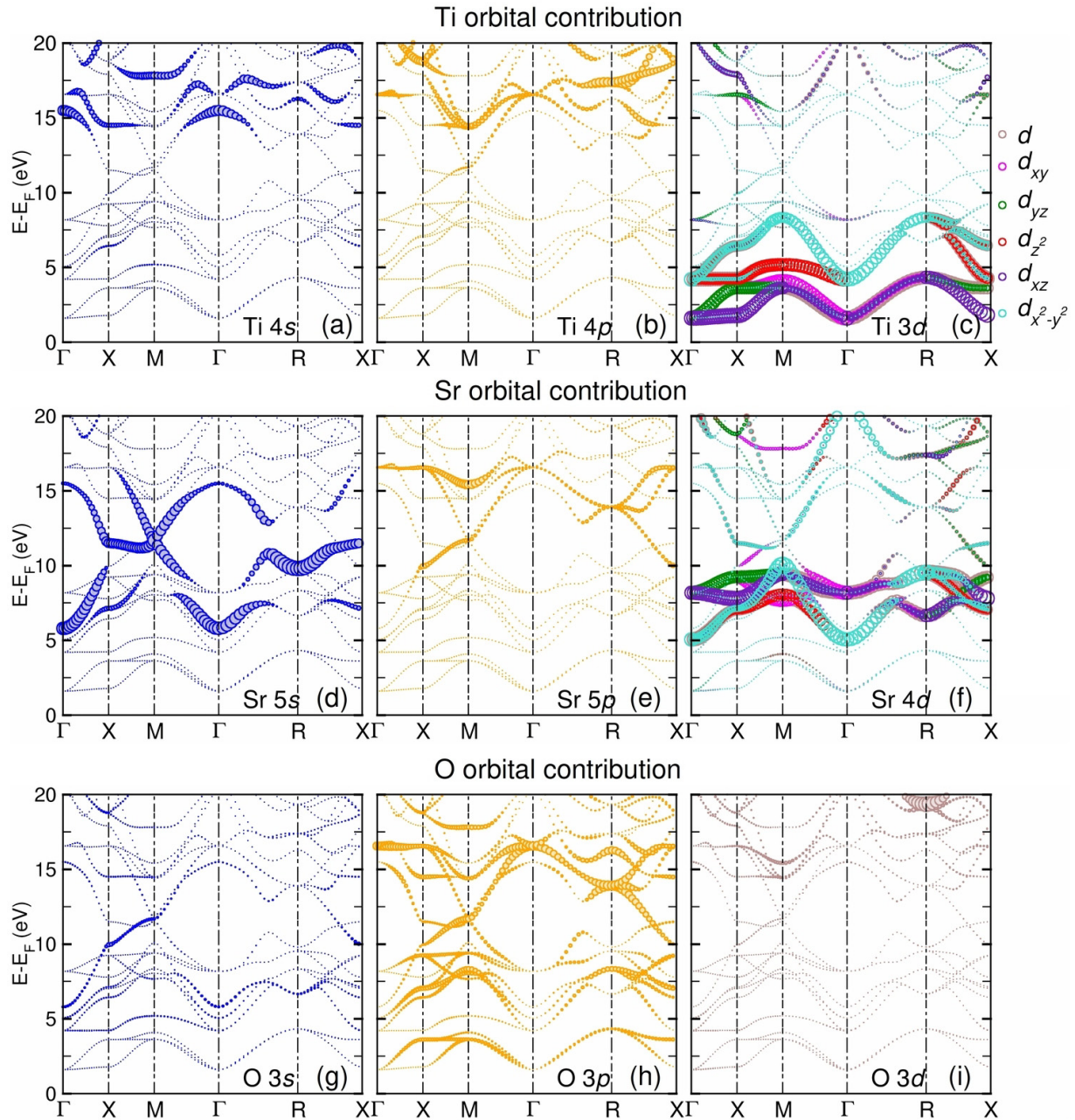


FIG. 1. (a)–(c) Ti, (d)–(f) Sr, and (g)–(i) O orbital-resolved contributions projected on the ground-state band structure obtained with VASP.

contributions from Ti  $3s$  and  $3p$  states over the entire Brillouin zone [Figs. 1(a) and 1(b)].

The Sr  $4d$  states [see Figs. 1(d)–1(f)] are predominant in the energy range 5–10 eV along the entire  $k$  path with strong hybridization with Sr  $5s$  states that extend from 5 to 16 eV. A weaker Sr  $5p$  contribution is observed above 15 eV, predominantly along  $X$ - $M$ - $\Gamma$  and  $R$ - $X$ .

Lastly, the contribution of the O ions is presented in Figs. 1(g)–1(i). The O  $3s$  states are mainly observed in the energy range 5–12 eV, prevailing along  $\Gamma$ - $X$ - $M$ . Moreover, mixed Sr  $5s$  and O  $3s$  character arises from 12 to 15 eV, consistent with Sponza *et al.* [35]. Furthermore, the O  $3p$  states have a predominant contribution up to 12 eV along  $X$ - $M$ , around  $R$  at  $\sim 13$  eV and around  $\Gamma$  at  $\sim 17$  eV. The contributions

around the conduction band minimum are expected to be of O  $2p$  nature due to hybridization effects with Ti  $3d$  states. We will refer to these contributions later to analyze the origin of prominent peaks in the XAS spectra in reciprocal space, similar to the previous study of MgO [36].

#### IV. X-RAY ABSORPTION SPECTRA

We now turn to the x-ray absorption spectra of the Ti  $L_{2,3}$  and O  $K$  edges in bulk SrTiO<sub>3</sub>. The ground-state calculations were performed with the PBEsol exchange-correlation functional, and the excitonic corrections were accounted for by solving BSE using the EXCITING code [26]. A total of 20 unoccupied bands for the O  $K$  edge and ten unoccupied



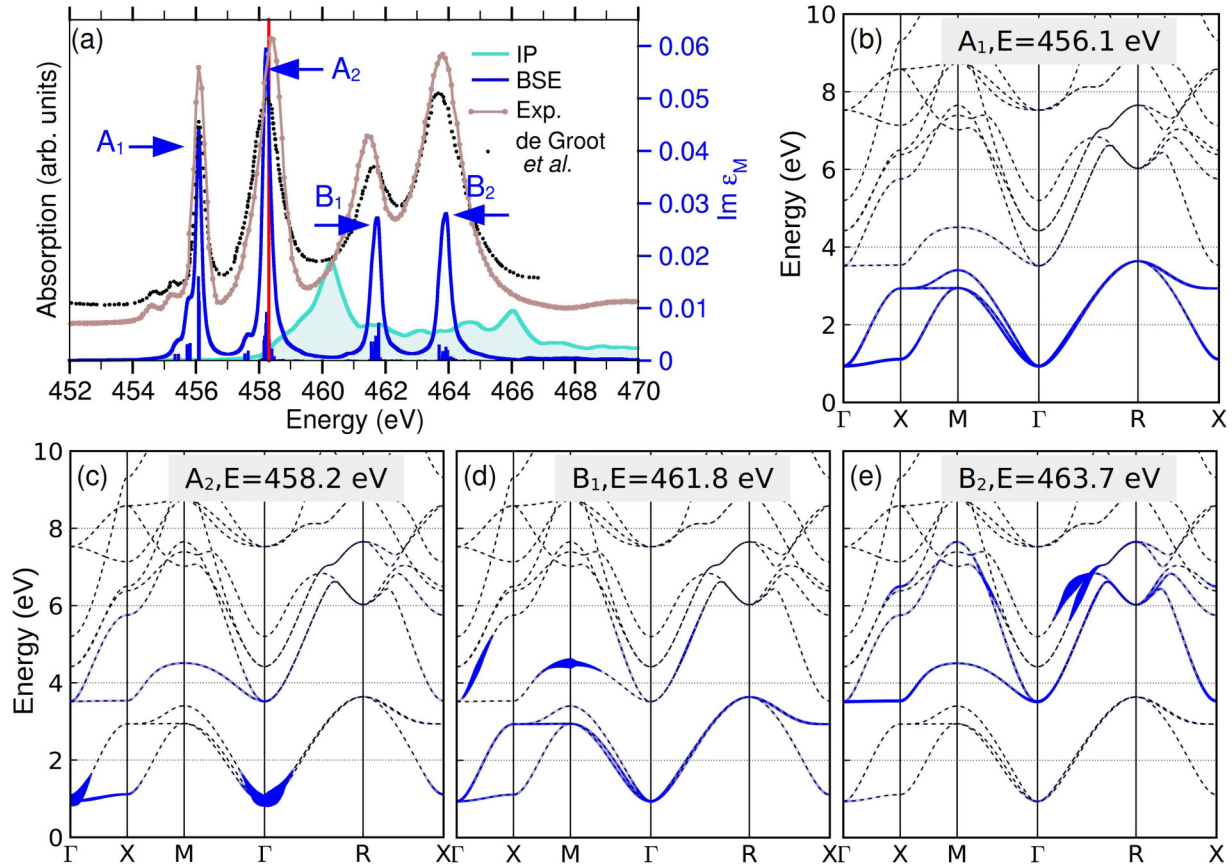


FIG. 2. XAS spectrum of the Ti  $L_{2,3}$  edge employing BSE to assess the excitonic effects: (a) calculated absorption spectra with BSE (blue line) and within the independent-particle approximation (cyan-shaded area) are compared with the experimental data from this study (brown line) and from Ref. [7] (black dots). A shift of 20.4 eV was applied to the calculated spectra to align the BSE spectrum with the first peak of the experiment [7], and a Lorentzian broadening of 0.10 eV is adopted to mimic the excitation lifetime. The red line marks the lowest transition in the IP approximation, and below this energy bound excitons are present. The blue vertical bars represent the oscillator strength (arb. units). (b)–(e) Excitonic contributions to the final states in the CB for the peaks marked in (a).

bands for the Ti  $L_{2,3}$  edge were employed to perform the BSE calculation, which were found to be sufficient to achieve a good agreement with experiment.

### A. Ti $L_{2,3}$ -edge XAS

#### Analysis in reciprocal space

The theoretical XAS spectrum of the Ti  $L_{2,3}$  edge is plotted in Fig. 2(a) together with the experimental one and previous experimental data from Refs. [6,7]. As the core energies obtained from DFT are not corrected, the BSE spectrum is shifted by 20.4 eV to align the first peak with the experimental data from Ref. [7], as done in earlier works [36–38]. This shift is applied also to the independent-particle (IP) spectrum to make the significant spectral weight redistribution due to BSE visible.

The Bethe-Salpeter equation represents a two-particle Schrödinger equation for the electron-hole pair [39,40]:

$$\sum_{\alpha'\beta'\mathbf{k}'} H_{\alpha\beta\mathbf{k},\alpha'\beta'\mathbf{k}'}^e A_{\alpha'\beta'\mathbf{k}'}^\lambda = E^\lambda A_{\alpha\beta\mathbf{k}}^\lambda, \quad (1)$$

where  $E^\lambda$  are the exciton energies and  $A_{\alpha\beta\mathbf{k}}^\lambda$  are the corresponding coupling coefficients between the electron and hole.

The indices  $\alpha, \beta, \mathbf{k}$  represent the core state, unoccupied state, and wave vector inside the first Brillouin zone, respectively. Furthermore, the effective  $e$ - $h$  Hamiltonian,  $H^{e-h}$ , consists of three terms [39,40],

$$H^{e-h} = H^{\text{diag}} + H^{\text{dir}} + 2H^{\text{x}}. \quad (2)$$

Here,  $H^{\text{diag}}$  contains the energy difference between the single-particle  $\alpha$  and  $\beta$  states, and  $H^{\text{dir}}$  is the attractive term that describes the direct  $e$ - $h$  interaction, which involves the statically screened Coulomb interaction  $W$  that is responsible for the bound core-exciton states. The last term,  $H^{\text{x}}$ , is repulsive in nature and gives the  $e$ - $h$  exchange interaction (involving the short-range bare Coulomb potential  $\bar{v}$ ), which accounts only for spin singlet excitations. Additionally, the second and third terms have opposite signs and lead to a red- and blueshift of the final BSE spectrum, respectively.

The IP spectrum is calculated by considering only the first term in Eq. (2), and it neglects any interaction between the core-hole and the electron. Subsequently, the spectrum within the IP picture [see Fig. 2(a)] fails to capture the four-peak feature. A good concurrence with experiment concerning the spectral shape and the relative positions of the prominent peaks at 456.1, 458.2, 461.8, and 463.7 eV denoted as  $A_1, A_2, B_1,$  and  $B_2$ , respectively, is obtained only after including

the excitonic effects, by considering all three terms in Eq. (2). Moreover, the relative intensities of the peaks are also rendered in better agreement with experiment. The emergence and characteristic splitting of the  $L_2$  and  $L_3$  edge, and the large redistribution of the spectral weight, highlight the strong excitonic effects. The crucial contribution of the attractive interaction between the core hole and the excited electron expressed in the direct term in Eq. (2) is responsible for the excitonic peaks. The calculated spectrum is also consistent with earlier work of Laskowski and Blaha [21]. The reduced intensity of the third ( $B_1$ ) and fourth ( $B_2$ ) peak in the calculated BSE spectrum is attributed to the local-field effects (LFE) and the finite cutoff of  $8.0a_0^{-1}$  for the  $|\mathbf{G}+\mathbf{q}|_{\max}$ . A detailed discussion of their influence and the role of the exchange term in Eq. (2) can be found in Appendix.

The  $L_{2,3}$  edge is comprised of strong electric dipole transitions,  $2p^63d^n \rightarrow 2p^53d^{n+1}$ . Due to spin-orbit coupling, the  $2p$  levels are split into  $2p_{1/2}$  and  $2p_{3/2}$  levels. A measure of this splitting is the separation between the  $L_2$  and  $L_3$  edges, calculated as  $B_2-A_2$ . We obtain 5.5 eV, in very good agreement with the measured value of 5.4 eV [8] and the calculated value of 5.65 [21] and 5.7 eV [22]. Furthermore, within each edge the peaks are separated by approximately 2.1 eV ( $A_2-A_1$ ), and 1.9 eV ( $B_2-B_1$ ), which is comparable with 2.3 eV [8], 2.2 eV [23], and 2.4 eV [21], and it reflects the crystal-field splitting of the  $t_{2g}$  and  $e_g$  states. Following Ref. [41], the branching ratio is calculated as the area under the  $L_3$  peak divided by the sum of the areas below  $L_2$  and  $L_3$ . We obtain 0.58, which is slightly higher than the experimental value of 0.47 [7]. Alternatively, the ratio of the areas below the  $L_2$  and  $L_3$  edges is 1 : 1.38, compared to approximately 1 : 1 [21] and 1.14 : 1 [7].

The BSE spectrum is characterized by four prominent peaks with high oscillator strength [see Fig. 2(a)]. Their origin in terms of transitions to the conduction bands is visualized in Figs. 2(b)–2(e). The corresponding electron-hole coupling coefficients from the BSE effective two-particle Hamiltonian [30,42] for a particular transition are displayed as circles in the band structure whose size scales with the magnitude. The  $A_1$  peak at 456.1 eV with a high oscillator strength originates from transition to the lowest unoccupied bands with Ti  $t_{2g}$  character [cf. Fig. 2(b)]. The  $A_2$  peak at 458.2 eV results from transitions to the lowest Ti  $t_{2g}$  bands at  $\Gamma$  and along  $\Gamma$ - $X$  with some admixture of transitions to  $e_g$  states [see Fig. 2(c)] along  $\Gamma$ - $X$ - $M$ - $\Gamma$ - $R$ . The  $B_1$  peak at 461.8 eV comprises transitions to the conduction bands with Ti  $t_{2g}$  character along the entire  $k$  path and  $e_g$  character around  $M$  and along  $\Gamma$ - $X$  [see Fig. 2(d)]. The final peak  $B_2$  at 463.7 eV arises from transitions to dispersive Ti  $d_{z^2}$  states along the entire  $k$  path in the energy range 3.5–7 eV [see Fig. 2(e)] as well as bands with mixed Sr  $e_g$  and  $5s$  states [see Figs. 1(d) and 1(f)].

The binding energies of  $A_1$  (2.3 eV) and  $A_2$  ( $\sim 100$  meV) [see Fig. 2(a)] differ by an order of magnitude. Laskowski and Blaha [21] have attributed the splitting of the peaks in the edge to this large difference in the exciton binding energies. However, as will be shown in the next section, the two excitons possess distinct orbital character,  $t_{2g}$  versus  $e_g$ , consistent with previous interpretations.

While the peak positions are excellently reproduced compared to experiment, there are differences concerning the shape and broadening of peaks. In particular, the prepeak

features in the Ti  $L_3$  spectrum are reproduced only for a broadening of 0.1 eV and obscured for larger values. In general, the lifetime of a photoelectron decreases with increasing excitation energy, and the broadening steadily increases over an energy scale set by the plasmon energy [33]. The stronger broadening of the  $L_2$  peaks compared to the  $L_3$  peaks in the experiment has been associated with the additional Coster-Kronig deexcitation channel [8]. Furthermore, Gilmore and Shirley [32] indicated that vibrational broadening is responsible for the augmented widths of the peaks with final-state  $e_g$  transition, i.e.,  $A_2$  and  $B_2$ . Many of the theoretical approaches, including the present work, employ a constant lifetime broadening resulting in the underestimation of the broadening of the peaks, in particular for the  $L_2$  edge [21,22,43]. This can be overcome by employing varied broadening for different energy ranges [33,43].

## B. Analysis of Ti $L_{2,3}$ edge excitons in real and reciprocal space

In Fig. 2(a) the red line at 458.3 eV marks the energy below which bound excitons are observed. The first bound exciton for the Ti  $L_{2,3}$  edge is at 455.3 eV with a substantial binding energy of  $-3.0$  eV, whereas the exciton at 458.2 eV has a much lower binding energy of  $-100$  meV. Similar binding energies were also calculated for the Ti  $L_{2,3}$  edge in the study of bulk SrTiO<sub>3</sub>, and for anatase and rutile TiO<sub>2</sub> in Ref. [21]. For the Ti  $L_{2,3}$  edge we analyze the first bound exciton at 455.3 eV and the exciton at 458.2 eV (see Fig. 3) both in reciprocal and in real space by plotting the real-space projection of the electronic part of the exciton wave function for a fixed hole. For similar analysis on other materials, see Refs. [30,38]. The first bound exciton [see Fig. 3(a)] arises from transitions to the lowest conduction band and is delocalized throughout the  $k$  path. Simultaneously, the real-space spread of the wave function in Figs. 3(b) and 3(c) is strongly localized and confined to essentially one unit cell. Moreover, we observe unambiguous  $t_{2g}$  and  $p_\pi$  character near the Ti and oxygen sites, respectively. This illustrates the hybridization between the Ti  $t_{2g}$  and O  $p$  states consistent with the orbital contribution in Fig. 1.

On the other hand, the exciton at 458.2 eV stems from transitions to unoccupied bands with mixed Ti  $t_{2g}$  and  $e_g$  character. Although we observe significant Ti  $t_{2g}$  character in reciprocal space [see Fig. 3(d)], the real-space projection shows a pronounced  $e_g$  character at the Ti sites [see Fig. 3(f)] at the center of the spread. In addition, while in reciprocal space the exciton is strongly localized around  $\Gamma$ , in real space it extends up to three unit cells [see Fig. 3(e)].

## C. O *K* edge XAS

### Analysis in reciprocal space

The calculated O *K* edge x-ray absorption spectrum obtained within the IP approximation and by including the electron- (core) hole interactions by solving the BSE is displayed in Fig. 4(a) together with the experimental data from the current study and from Ref. [10] for comparison. A shift of 26.5 eV is applied to the calculated spectra to align the energetic position of the first peak in the BSE spectrum with the experimental spectrum [10], and the same shift is applied

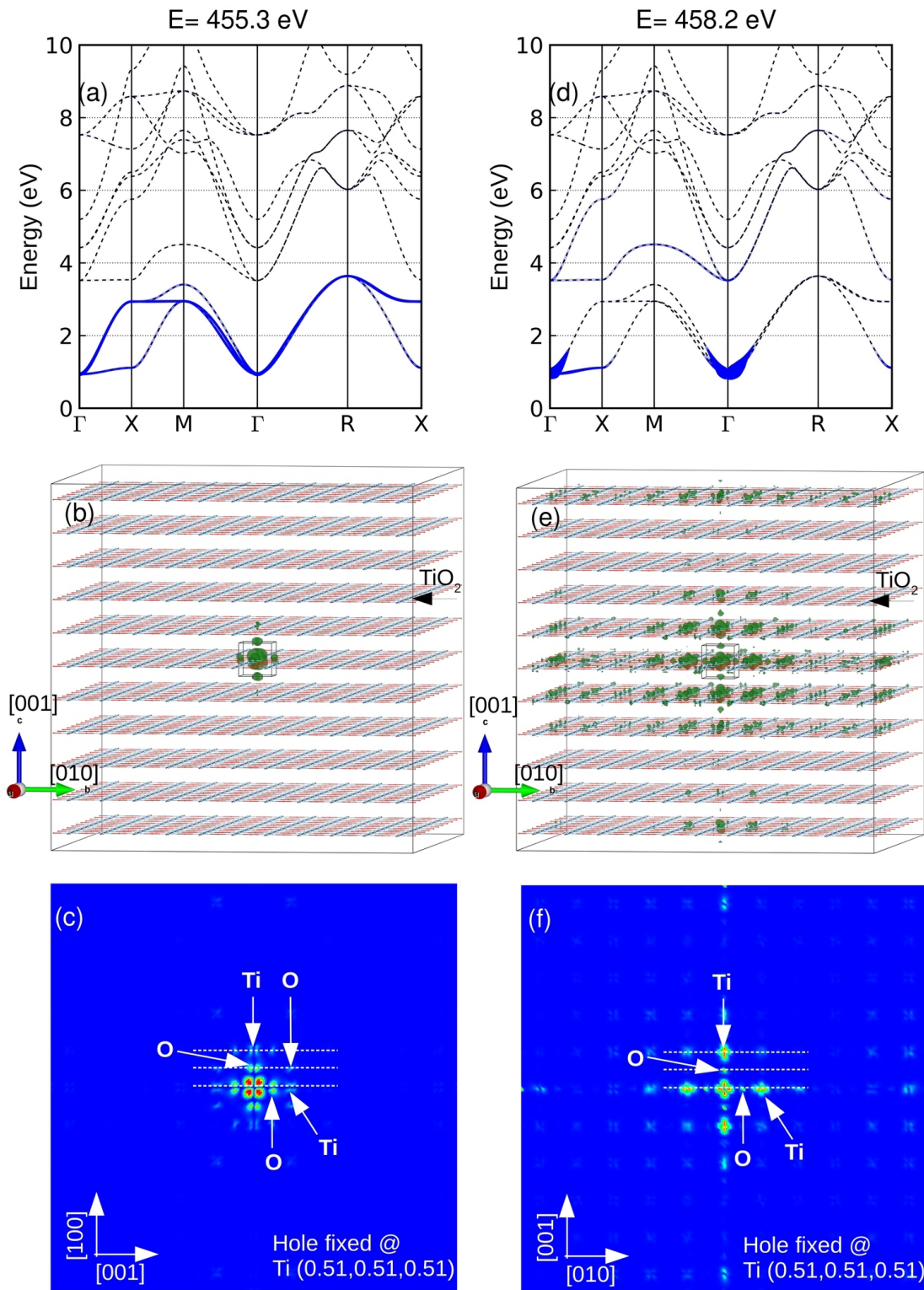


FIG. 3. Ti  $L_{2,3}$  edge: (a), (d) main contribution of the excitons in reciprocal space. (b), (e) 3D distribution of the real-space projection in the simulation box, where only the  $\text{TiO}_2$  layers are displayed for clarity. (c), (f) 2D projection of the density associated with the electronic part of the excitonic wave functions for a selected cross section, visualizing the spatial extension of the exciton. The hole is fixed near the Ti ion (fractional coordinate: 0.51, 0.51, 0.51).

to the IP spectrum to emphasize the substantial spectral weight redistribution due to excitonic effects.

Although the spectrum within the IP approximation reproduces the overall shape of the experimental spectrum, it is

only after including the electron- (core) hole interaction with BSE that we achieve the best agreement with experiment [see Fig. 4(a)]. Upon solving BSE, the redistribution of the spectral weight at the onset of the spectrum results in a high-intensity



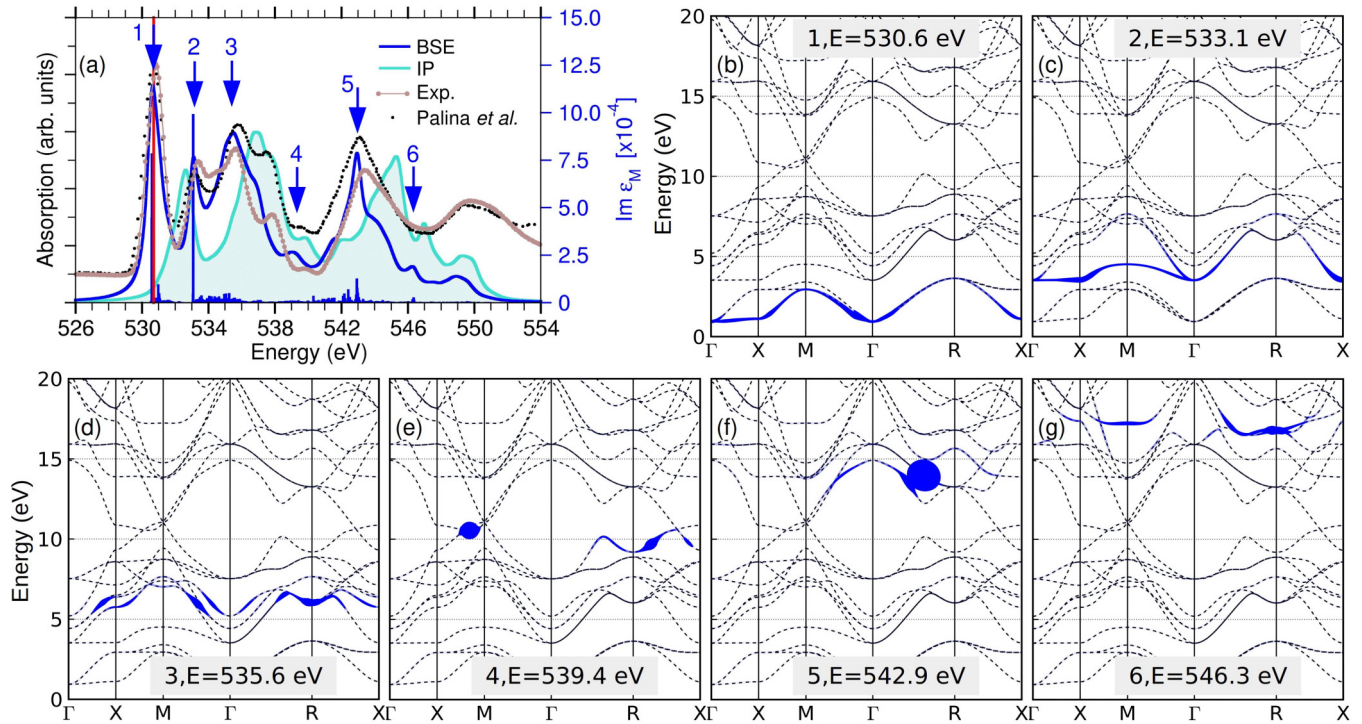


FIG. 4. XAS spectrum of the O  $K$  edge employing BSE corrections: (a) calculated absorption spectra with BSE (blue line) and within the IP approximation (cyan-shaded area) are compared with experimental data (brown line), and spectrum from Palina *et al.* [10] (black dots). A shift of 26.5 eV was applied to the calculated spectra to align to the first peak of experiment [10], and a Lorentzian broadening of 0.35 eV is adopted to mimic the excitation lifetime. The red line marks the energetic position below which bound excitons are present, and the blue vertical bars represent the oscillator strength (arb. units). (b)–(g) Excitonic contributions to the final states in the CB for the peaks marked in (a).

peak at 530.6 eV, followed by a second peak at 533.1 eV. This characteristic double peak is common for transition-metal oxides and is attributed to the transition-metal (TM)  $3d$ -O  $2p$  hybridization and, in particular, the TM  $t_{2g}$ - $e_g$  splitting in the octahedral coordination [14,15]. The BSE formalism correctly describes the photoexcitation of the many-electron system in contrast to the IP approximation, which only considers single-particle transitions and where only a single peak is present with a slight shoulder at higher energies. The leading contribution of the attractive  $e$ - $h$  correlations introduced by the nonlocality of the direct term in the BSE emphasizes the importance of screening, and results in the shifting of the oscillator strength and the formation of bound exciton states. The BSE spectrum is concurrent with experiment with respect to the energetic positions of the four prominent peaks at 530.6, 533.1, 535.6, and 542.9 eV, and with the previous BSE results of Liang *et al.* [15].

In Fig. 4(a) we have marked the six prominent peaks that are analyzed in reciprocal space [see Figs. 4(b)–4(g)] by plotting the electron-hole coupling coefficient from the BSE eigenvector in reciprocal space, analogous to Sec. IV A 1. Analysis of the transitions for the first prominent peak at 530.6 eV shows that these are delocalized along the Brillouin zone at the bottom of the CB and comprise predominantly Ti  $d_{xz}$  character. The second peak at 533.1 eV arises from transitions to the CB with Ti  $e_g$  character and is also delocalized throughout the entire  $k$  path. This analysis in reciprocal space clearly shows the distinct Ti  $t_{2g}$  and  $e_g$  orbital contribution for

the two peaks (530.6 and 533.1 eV). The subsequent peak at 535.6 eV stems from transitions to the CB with significant contributions from the Sr  $e_g$  states and mixed O  $3p$ , Sr  $e_g$ , and Sr  $5s$  states along  $\Gamma$ - $X$ - $M$ - $\Gamma$ - $R$ . The transitions to Sr  $4d$  states are consistent with previous experimental assignment [17], and they substantiate our analysis. Furthermore, the peak at 539.4 eV results from transitions to unoccupied bands with predominant Sr  $5s$  character hybridized with Sr  $d_{xz}$  states along  $\Gamma$ - $R$ - $X$  and mixed O  $3p$ , Sr  $4s$ , and Sr  $d_{x^2-y^2}$  along  $X$ - $M$  [see Figs. 1(h), 1(d), and 1(f), respectively]. The peak at 542.9 eV is due to transitions to higher-lying CB with predominant Sr  $5s$  hybridized with Sr  $5p$  and Sr  $d_{x^2-y^2}$  [see Figs. 1(d)–1(f)]. In addition, there are contributions from Ti  $4s$  and  $4p$ , and O  $3p$  states in this energy range. The final peak at 456.3 eV is comprised of transitions to CB above 16 eV with mixed contributions from Ti  $4s$ , Sr  $d_{xz}$ , and O  $3p$  states along  $X$ - $M$ - $\Gamma$  and Sr  $t_{2g}$  states along  $\Gamma$ - $R$ - $X$ .

#### D. Analysis of O $K$ excitons in real and reciprocal space

Similar to the  $L_{2,3}$  edge, bound excitons are found at energies below 530.7 eV marked by the red line in Fig. 4(a). The first bound exciton is at 530.24 eV with a binding energy of around  $-470$  meV. Similar binding energies were calculated for the O  $K$  edge of oxides such as  $\text{Ga}_2\text{O}_3$  [44,45] and  $\text{MgO}$  [36]. The second exciton at 533.1 eV is nonbound (2.4 eV). The analysis in reciprocal space in Fig. 5(a) shows that the first bound exciton results from transitions to the bottom of the CB

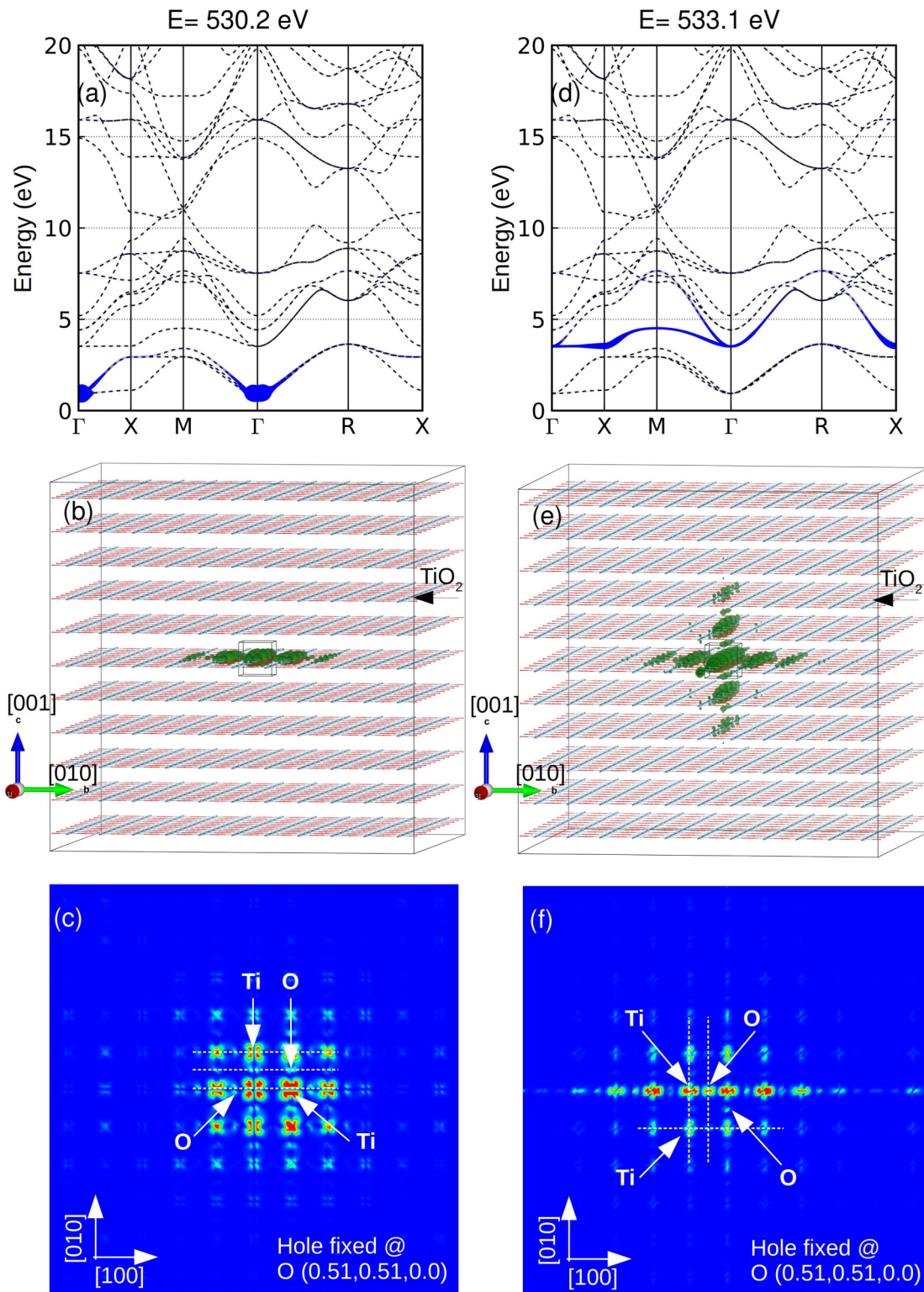


FIG. 5. O  $K$  edge: (a), (d) Contribution of the excitons in reciprocal space, (b), (e) 3D distribution of the real-space projection in the simulation box, and (c), (f) cross section of the density distribution associated with the electronic part of the excitonic wave functions in real space. The hole is fixed near the oxygen (fractional coordinate: 0.51, 0.51, 0.00).

and is strongly localized around  $\Gamma$ . In addition, weak transitions are also observed along  $\Gamma$ - $X$ . The participating CB have predominantly Ti  $t_{2g}$  character hybridized with O  $3p$  along the entire  $k$  path. The real-space projections of the excitonic wave function, namely the 3D spread and a two-dimensional cross

section through the  $\text{TiO}_2$  plane, are plotted in Figs. 5(b) and 5(c), respectively. Here, the hole was fixed near the oxygen (fractional coordinate: 0.51, 0.51, 0.00). Variation of this position did not modify visibly the electronic part of the exciton wave function. We observe a large contribution from the Ti



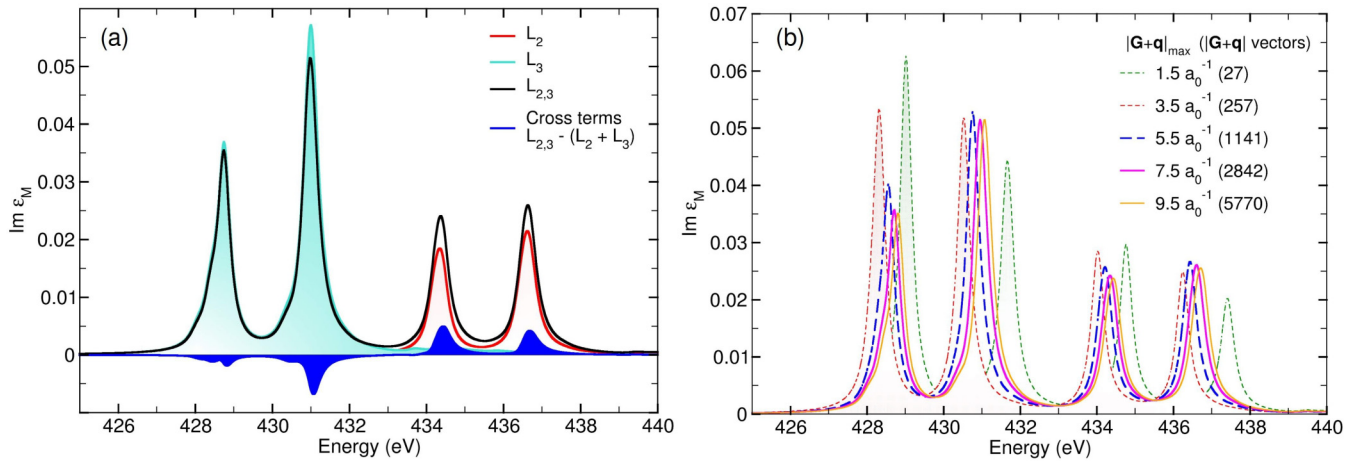


FIG. 6. Ti  $L_{2,3}$  edge: (a) Spectra obtained including only Ti  $2p_{1/2}$  ( $L_2$ ) and Ti  $2p_{3/2}$  ( $L_3$ ) as initial states. The *cross terms*,  $L_{2,3} - (L_2 + L_3)$ , are also shown for comparison. (b) Influence of the magnitude of the  $|\mathbf{G} + \mathbf{q}|$  vectors to account for local field effects. Note that here a Lorentzian broadening of 0.2 eV was used.

$t_{2g}$  states extending up to four unit cells, as well as from O  $3p_\pi$  states near the O sites, consistent with our analysis in reciprocal space, as well as with previous orbital mapping from electron energy-loss spectroscopy (EELS) measurement [16]. The spread of the wave function in the  $x$ - $y$  plane indicates the presence of substantial hybridization of the Ti  $t_{2g}$ -O  $p$  states. In addition, the 3D visualization presented in Fig. 5(b) brings out an intriguing feature, i.e., the spread of the wave function is two-dimensional, confined in the  $x$ - $y$  plane. While the origin of this two-dimensional anisotropy requires further investigation, it may have important consequences for applications. The real-space projection of the exciton suggests an intermediate character between the Wannier and Frenkel limits, i.e., a charge-transfer (CT) type, characterized by the spread of the wave function over a few unit cells along [100] and [010].

The second nonbound exciton at 533.1 eV stems from transitions to CB in the energy range of 3–7 eV, and the contributions are dispersive throughout the  $k$  path [see Fig. 5(d)]. From the orbital-resolved band structure in Figs. 1(c) and 1(h), we infer that the bands have predominantly Ti  $e_g$  character mixed with O  $3p$  orbitals. The real-space wave function spread in Fig. 5(e) is confined to two orthogonal planes: (001) and (010). The two-dimensional projection renders strong  $e_g$  character near Ti sites along with O  $p_\sigma$  character near the O sites [see Fig. 5(f)], consistent with a recent EELS analysis [16].

## V. CONCLUSION

The O  $K$  edge and Ti  $L_{2,3}$  edge XAS spectra of bulk SrTiO<sub>3</sub> were calculated using DFT and considering many-body effects by solving the Bethe-Salpeter equation. Both XAS spectra agree very well with experiment with respect to the energetic positions and relative intensities of the prominent peaks, underlying the importance of taking into account the electron- (core) hole interactions. Moreover, we provide a thorough analysis of the origin of the relevant peaks in the spectra and, in particular, the transitions to the unoccupied

bands in reciprocal space. For the Ti  $L_{2,3}$  edge, the analysis of the origin of the four prominent peaks in reciprocal space confirm the transitions from  $2p_{1/2}$  to the CB with Ti  $3d t_{2g}$  (456.1 eV) and Ti  $3d e_g$  (458.2 eV) character and from  $2p_{3/2}$  to Ti  $3d t_{2g}$  (461.8 eV) and Ti  $3d e_g$  (463.7 eV), respectively. The real-space projection of the first bound exciton reveals a strongly localized spread of the exciton wave function confined to 1–2 unit cells with  $t_{2g}$  character near the Ti and  $3p$  character near the oxygen sites. This goes hand in hand with the delocalization along the entire  $k$  path in reciprocal space. For the O  $K$  edge spectrum, the first two peaks with high oscillator strength at 530.6 and 533.1 eV stem from transitions to CB with Ti  $d_{xz}$  and  $e_g$  character, respectively, and they are delocalized throughout the entire  $k$  path. In addition, the real-space projection of the exciton wave function for the first bound exciton at 530.24 eV shows a strong two-dimensional (2D) nature with predominant  $t_{2g}$  states near the Ti sites, and  $2p_\pi$  states near the O sites, and it is identified as a charge-transfer type of exciton. A similar 2D spread for the bound exciton was observed in the optical spectrum of anatase TiO<sub>2</sub> at 3.79 eV [46,47]. We note that 2D excitons have been previously reported in layered 2D materials, for example, transition-metal dichalcogenides [48,49] and hexagonal boron nitride [50], which is consistent with the 2D lattice structure. The intriguing appearance of a 2D exciton in a 3D lattice found in this work calls for further investigations of, e.g., the influence of external stimuli such as mechanical strain or light. Furthermore, the emergent physics at the surface or interface of SrTiO<sub>3</sub>-based heterostructures [51–55], such as the two-dimensional electron gas, calls for a thorough analysis of many-body effects, in particular concerning the potential exciton formation in spatially separated but coupled electron-hole-bilayers [53,56].

## ACKNOWLEDGMENTS

We thank Heiko Wende for fruitful discussions, and Florin Radu, Kai Chen, and Chen Luo for experimental support during the beamtime at BESSY II. We wish to

acknowledge funding by the Deutsche Forschungsgemeinschaft (DFG, German Research Foundation) within collaborative research center CRC1242 (Project No. 278162697, subprojects C02 and A07) and computational time at the Center for Computational Sciences and Simulation of the University of Duisburg-Essen on the supercomputer magnitude (DFG Grants No. INST 20876/209-1 FUGG and No. INST 20876/243-1 FUGG). Additionally, B.E. acknowledges funding through the Project No. 322462997 (MUMAGI II) financed by the DFG. Helmholtz Zentrum Berlin is gratefully acknowledged for the allocation of synchrotron radiation beamtime under the Proposal No. 192-08508-ST/R. We acknowledge support by the Open Access Publication Fund of the University of Duisburg-Essen.

#### APPENDIX: INFLUENCE OF LOCAL-FIELD EFFECTS AND CROSS TERMS

We briefly discuss the role of mixing between the two initial core states, Ti  $2p_{3/2}$  and Ti  $2p_{1/2}$ , on the overall Ti  $L_{2,3}$  spectrum, and the influence of local-field effects. In Fig. 6(a) we plot the Ti  $L_{2,3}$ , and the separate contributions of the  $L_2, L_3$  spectra. The so-called *cross terms* are evaluated as  $[L_{2,3} - (L_2 + L_3)]$  (blue solid area), and they indicate that a fraction of the intensity of the  $L_3$  subedge is transferred to the  $L_2$  edge. The substantial effect of coherent mixing of excitations from the  $2p_{1/2}$  and  $2p_{3/2}$  states on the branching

ratio was also observed in the work of Laskowski and Blaha [21]. Overall, their effect is quite significant in bulk SrTiO<sub>3</sub>, as was found also in other oxides such as CaO [37,41].

To study the local-field effects (LFE) on the Ti  $L_{2,3}$  spectrum, we calculate the spectrum by varying the Coulomb potential between the core-hole and electron described by the  $|\mathbf{G}+\mathbf{q}|_{\max}$  parameter [see Fig. 6(b)]. We already get a good agreement with experiment with respect to the spectral features with 27  $|\mathbf{G}+\mathbf{q}|$  vectors (cutoff of  $|\mathbf{G}+\mathbf{q}|_{\max} = 1.5a_0^{-1}$ ). However, the relative intensity of the peaks is not well described compared to the experiment. The intermediate values of  $|\mathbf{G}+\mathbf{q}|_{\max}$  realize satisfactorily the screened Coulomb interaction between core-hole and electron. Furthermore, as the exchange interaction mixes the transition of the subedges, illustrated by the cross terms in Fig. 6(a), we observe that the relative intensity of the peaks is only reproduced at high values for  $|\mathbf{G}+\mathbf{q}|_{\max}$ . Thus, upon increasing the  $|\mathbf{G}+\mathbf{q}|_{\max}$  cutoff to  $7.5a_0^{-1}$ , we obtain spectra with an improved agreement with experiment regarding the intensity of the  $L_2$  edge. The trend elucidates that the nonlocal repulsive exchange part [third term in Eq. (2)] is paramount to reproducing the relative intensities of the peaks. Increasing the cutoff further to  $9.5a_0^{-1}$  has a negligible effect on the intensity. We note that even at such high values of  $|\mathbf{G}+\mathbf{q}|_{\max}$ , the relative intensity of the  $L_2$  edge remains underestimated, but increasing the cutoff dramatically increases the memory requirement, rendering the calculation infeasible. Thus, we proceed with a cutoff to  $8.0a_0^{-1}$  for the calculation of the Ti  $L_{2,3}$  spectrum.

- 
- [1] J. Mannhart and D. G. Schlom, Oxide interfaces-An opportunity for electronics, *Science* **327**, 1607 (2010).
- [2] A. F. Santander-Syro, T. K. O. Copie, F. Fortuna, S. Pailh s, R. Weht, X. G. Qiu, F. Bertran, A. Nicolaou, A. Taleb-Ibrahimi, P. L. F vre, G. Herranz, M. Bibes, N. Reyren, Y. Apertet, P. Lecoeur, A. Barth l my, and M. J. Rozenberg, Two-dimensional electron gas with universal subbands at the surface of SrTiO<sub>3</sub>, *Nature (London)* **469**, 189 (2011).
- [3] W. Meevasana, P. D. C. King, R. H. He, S.-K. Mo, M. Hashimoto, A. Tama, P. Songiririthigul, F. Baumberger, and Z.-X. Shen, Creation and control of a two-dimensional electron liquid at the bare SrTiO<sub>3</sub> surface, *Nat. Mater.* **10**, 114 (2011).
- [4] L. Li, C. Richter, J. Mannhart, and R. C. Ashoori, Coexistence of magnetic order and two-dimensional superconductivity at LaAlO<sub>3</sub>/SrTiO<sub>3</sub> interfaces, *Nat. Phys.* **7**, 762 (2011).
- [5] G. van der Laan, Polaronic satellites in x-ray-absorption spectra, *Phys. Rev. B* **41**, 12366 (1990).
- [6] M. Abbate, F. M. F. de Groot, J. C. Fuggle, A. Fujimori, Y. Tokura, Y. Fujishima, O. Strebel, M. Domke, G. Kaindl, J. van Elp, B. T. Thole, G. A. Sawatzky, M. Sacchi, and N. Tsuda, Soft-x-ray-absorption studies of the location of extra charges induced by substitution in controlled-valence materials, *Phys. Rev. B* **44**, 5419 (1991).
- [7] F. M. F. de Groot, M. O. Figueiredo, M. J. Basto, M. Abbate, H. Petersen, and J. C. Fuggle, 2p x-ray absorption of titanium in minerals, *Phys. Chem. Miner.* **19**, 140 (1992).
- [8] Y. Uehara, D. Lindle, T. Callcott, L. Terminello, F. Himpsel, D. Ederer, J. Underwood, E. Gullikson, and R. Perera, Resonant inelastic scattering at the  $L$  edge of Ti in barium strontium titanate by soft x-ray fluorescence spectroscopy, *Appl. Phys. A* **65**, 179 (1997).
- [9] J. Schlappa, C. F. Chang, Z. Hu, E. Schierle, H. Ott, E. Weschke, G. Kaindl, M. Huijben, G. Rijnders, D. H. A. Blank, L. H. Tjeng, and C. Sch blier-Langeheine, Resonant soft x-ray scattering from stepped surfaces of SrTiO<sub>3</sub>, *J. Phys.: Condens. Matter* **24**, 035501 (2012).
- [10] N. Palina, A. Annadi, T. C. Asmara, C. Diao, X. Yu, M. B. H. Breese, T. Venkatesan, Ariando, and A. Rusydi, Electronic defect states at the LaAlO<sub>3</sub>/SrTiO<sub>3</sub> heterointerface revealed by O K-edge x-ray absorption spectroscopy, *Phys. Chem. Chem. Phys.* **18**, 13844 (2016).
- [11] M. Salluzzo, in *Oxide Thin Films, Multilayers, and Nanocomposites*, edited by P. Mele, T. Endo, S. Arisawa, C. Li, and T. Tsuchiya (Springer International, Cham, 2015), pp. 181–211.
- [12] O. Lobacheva, M. Chavarha, Y. M. Yiu, T. K. Sham, and L. V. Goncharova, The local structure and ferromagnetism in Fe-implanted SrTiO<sub>3</sub> single crystals, *J. Appl. Phys.* **116**, 013901 (2014).
- [13] G. S. Henderson, F. M. de Groot, and B. J. Moulton, X-ray absorption near-edge structure (XANES) spectroscopy, *Rev. Mineral. Geochem.* **78**, 75 (2014).
- [14] F. M. F. de Groot, J. Faber, J. J. M. Michiels, M. T. Czy zyk, M. Abbate, and J. C. Fuggle, Oxygen 1s x-ray absorption of tetravalent titanium oxides: A comparison with single-particle calculations, *Phys. Rev. B* **48**, 2074 (1993).
- [15] Y. Liang, J. Vinson, S. Pemmaraju, W. S. Drisdell, E. L. Shirley, and D. Prendergast, Accurate X-Ray Spectral Predictions: An

- Advanced Self-Consistent-Field Approach Inspired by Many-Body Perturbation Theory, *Phys. Rev. Lett.* **118**, 096402 (2017).
- [16] C. Iwashimizu, M. Haruta, and H. Kurata, Electron orbital mapping of SrTiO<sub>3</sub> using electron energy-loss spectroscopy, *Appl. Phys. Lett.* **119**, 232902 (2021).
- [17] F. Frati, M. O. J. Y. Hunault, and F. M. F. de Groot, Oxygen K-edge x-ray absorption spectra, *Chem. Rev.* **120**, 4056 (2020).
- [18] P. Krüger and C. R. Natoli, X-ray absorption spectra at the Ca L<sub>2,3</sub> edge calculated within multichannel multiple scattering theory, *Phys. Rev. B* **70**, 245120 (2004).
- [19] F. M. de Groot, H. Elnaggar, F. Frati, R. pan Wang, M. U. Delgado-Jaime, M. van Veenendaal, J. Fernandez-Rodriguez, M. W. Haverkort, R. J. Green, G. van der Laan, Y. Kvashnin, A. Hariki, H. Ikeno, H. Ramanantoanina, C. Daul, B. Delley, M. Odelius, M. Lundberg, O. Kuhn, S. I. Bokarev *et al.*, 2p x-ray absorption spectroscopy of 3d transition metal systems, *J. Electron Spectrosc. Relat. Phenom.* **249**, 147061 (2021).
- [20] H. Ikeno, F. M. F. de Groot, E. Stavitski, and I. Tanaka, Multiplet calculations of L<sub>2,3</sub> x-ray absorption near-edge structures for 3d transition-metal compounds, *J. Phys.: Condens. Matter* **21**, 104208 (2009).
- [21] R. Laskowski and P. Blaha, Understanding the L<sub>2,3</sub> x-ray absorption spectra of early 3d transition elements, *Phys. Rev. B* **82**, 205104 (2010).
- [22] J. Vinson, J. J. Rehr, J. J. Kas, and E. L. Shirley, Bethe-salpeter equation calculations of core excitation spectra, *Phys. Rev. B* **83**, 115106 (2011).
- [23] J. C. Woicik, C. Weiland, C. Jaye, D. A. Fischer, A. K. Rumaiz, E. L. Shirley, J. J. Kas, and J. J. Rehr, Charge-transfer satellites and chemical bonding in photoemission and x-ray absorption of SrTiO<sub>3</sub> and rutile TiO<sub>2</sub>: Experiment and first-principles theory with general application to spectroscopic analysis, *Phys. Rev. B* **101**, 245119 (2020).
- [24] D. D. Ruiz and C. Cocchi, First-principles core spectroscopy of LiCoO<sub>2</sub> and CoO<sub>2</sub>, *J. Phys. Chem. C* **126**, 10949 (2022).
- [25] J. J. Kas, J. J. Rehr, and T. P. Devereaux, *ab initio* Multiplet-Plus-Cumulant Approach for Correlation Effects in X-Ray Photoelectron Spectroscopy, *Phys. Rev. Lett.* **128**, 216401 (2022).
- [26] A. Gulans, S. Kontur, C. Meisenbichler, D. Nabok, P. Pavone, S. Rigamonti, S. Sagmeister, U. Werner, and C. Draxl, Exciting: A full-potential all-electron package implementing density-functional theory and many-body perturbation theory, *J. Phys.: Condens. Matter* **26**, 363202 (2014).
- [27] J. P. Perdew, A. Ruzsinszky, G. I. Csonka, O. A. Vydrov, G. E. Scuseria, L. A. Constantin, X. Zhou, and K. Burke, Restoring the Density-Gradient Expansion for Exchange in Solids and Surfaces, *Phys. Rev. Lett.* **100**, 136406 (2008).
- [28] J. P. Perdew, A. Ruzsinszky, G. I. Csonka, O. A. Vydrov, G. E. Scuseria, L. A. Constantin, X. Zhou, and K. Burke, Erratum: Restoring the Density-Gradient Expansion for Exchange in Solids and Surfaces, *Phys. Rev. Lett.* **102**, 039902(E) (2009).
- [29] V. Begum, M. E. Gruner, and R. Pentcheva, Role of the exchange-correlation functional on the structural, electronic, and optical properties of cubic and tetragonal SrTiO<sub>3</sub> including many-body effects, *Phys. Rev. Mater.* **3**, 065004 (2019).
- [30] S. Sagmeister and C. Ambrosch-Draxl, Time-dependent density functional theory versus Bethe-Salpeter equation: An all-electron study, *Phys. Chem. Chem. Phys.* **11**, 4451 (2009).
- [31] S. M. Dancoff, Non-adiabatic meson theory of nuclear forces, *Phys. Rev.* **78**, 382 (1950).
- [32] K. Gilmore and E. L. Shirley, Numerical quantification of the vibronic broadening of the SrTiO<sub>3</sub> Ti L-edge spectrum, *J. Phys.: Condens. Matter* **22**, 315901 (2010).
- [33] J. Vinson, Advances in the OCEAN-3 spectroscopy package, *Phys. Chem. Chem. Phys.* **24**, 12787 (2022).
- [34] T. Noll and F. Radu, The mechanics of the vekmag experiment, *Proc. MEDSI2016*, 370 (2017).
- [35] L. Sponza, V. Véniard, F. Sottile, C. Giorgetti, and L. Reining, Role of localized electrons in electron-hole interaction: The case of SrTiO<sub>3</sub>, *Phys. Rev. B* **87**, 235102 (2013).
- [36] V. Begum, M. E. Gruner, C. Vorwerk, C. Draxl, and R. Pentcheva, Theoretical description of optical and x-ray absorption spectra of MgO including many-body effects, *Phys. Rev. B* **103**, 195128 (2021).
- [37] C. Vorwerk, C. Cocchi, and C. Draxl, Addressing electron-hole correlation in core excitations of solids: An all-electron many-body approach from first principles, *Phys. Rev. B* **95**, 155121 (2017).
- [38] C. Vorwerk, B. Aurich, C. Cocchi, and C. Draxl, Bethe-Salpeter equation for absorption and scattering spectroscopy: Implementation in the exciting code, *Electron. Struct.* **1**, 037001 (2019).
- [39] P. Puschnig and C. Ambrosch-Draxl, Optical absorption spectra of semiconductors and insulators including electron-hole correlations: An *ab initio* study within the LAPW method, *Phys. Rev. B* **66**, 165105 (2002).
- [40] W. Olovsson, I. Tanaka, T. Mizoguchi, P. Puschnig, and C. Ambrosch-Draxl, All-electron Bethe-Salpeter calculations for shallow-core x-ray absorption near-edge structures, *Phys. Rev. B* **79**, 041102(R) (2009).
- [41] P. S. Miedema, H. Ikeno, and F. M. F. de Groot, First principles multiplet calculations of the calcium L<sub>2,3</sub> x-ray absorption spectra of CaO and CaF<sub>2</sub>, *J. Phys.: Condens. Matter* **23**, 145501 (2011).
- [42] M. Rohlfing and S. G. Louie, Electron-hole excitations and optical spectra from first principles, *Phys. Rev. B* **62**, 4927 (2000).
- [43] T. Kroll, E. I. Solomon, and F. M. F. de Groot, Final-state projection method in charge-transfer multiplet calculations: An analysis of Ti L-Edge absorption spectra, *J. Phys. Chem. B* **119**, 13852 (2015).
- [44] C. Cocchi, H. Zschiesche, D. Nabok, A. Mogilatenko, M. Albrecht, Z. Galazka, H. Kirmse, C. Draxl, and C. T. Koch, Atomic signatures of local environment from core-level spectroscopy in β-Ga<sub>2</sub>O<sub>3</sub>, *Phys. Rev. B* **94**, 075147 (2016).
- [45] C. W. Vorwerk, Theoretical Spectroscopy of Ga<sub>2</sub>O<sub>3</sub>, Ph.D. thesis, Humboldt-Universität zu Berlin, Mathematisch-Naturwissenschaftliche Fakultät (2021).
- [46] E. Baldini, L. Chiodo, A. Dominguez, M. Palummo, S. Moser, M. Yazdi-Rizi, G. Auböck, B. Mallett, H. Berger, A. Magrez, C. Bernhard, M. Grioni, A. Rubio, and M. Chergui, Strongly bound excitons in anatase TiO<sub>2</sub> single crystals and nanoparticles, *Nat. Commun.* **8**, 13 (2016).
- [47] E. Baldini, T. Palmieri, A. Dominguez, A. Rubio, and M. Chergui, Giant Exciton Mott Density in Anatase TiO<sub>2</sub>, *Phys. Rev. Lett.* **125**, 116403 (2020).
- [48] D. Y. Qiu, F. H. da Jornada, and S. G. Louie, Optical Spectrum of MoS<sub>2</sub>: Many-body Effects and Diversity of Exciton States, *Phys. Rev. Lett.* **111**, 216805 (2013).



- [49] M. M. Ugeda, A. J. Bradley, S.-F. Shi, F. H. da Jornada, Y. Zhang, D. Y. Qiu, W. Ruan, S.-K. Mo, Z. Hussain, Z.-X. Shen, F. Wang, S. G. Louie, and M. F. Crommie, Giant bandgap renormalization and excitonic effects in a monolayer transition metal dichalcogenide semiconductor, *Nat. Mater.* **13**, 1091 (2014).
- [50] S. Galambosi, L. Wirtz, J. A. Soininen, J. Serrano, A. Marini, K. Watanabe, T. Taniguchi, S. Huotari, A. Rubio, and K. Hämäläinen, Anisotropic excitonic effects in the energy loss function of hexagonal boron nitride, *Phys. Rev. B* **83**, 081413(R) (2011).
- [51] A. Ohtomo and H. Y. Hwang, A high-mobility electron gas at the  $\text{LaAlO}_3/\text{SrTiO}_3$  heterointerface, *Nature (London)* **427**, 423 (2004).
- [52] N. Reyren, S. Thiel, A. D. Caviglia, L. F. Kourkoutis, G. Hammerl, C. Richter, C. W. Schneider, T. Kopp, A.-S. Rüetschi, D. Jaccard, M. Gabay, D. A. Muller, J.-M. Triscone, and J. Mannhart, Superconducting interfaces between insulating oxides, *Science* **317**, 1196 (2007).
- [53] R. Pentcheva and W. E. Pickett, Avoiding the Polarization Catastrophe in  $\text{LaAlO}_3$  Overlayers on  $\text{SrTiO}_3(001)$  Through Polar Distortion, *Phys. Rev. Lett.* **102**, 107602 (2009).
- [54] B. Geisler and R. Pentcheva, Fundamental difference in the electronic reconstruction of infinite-layer versus perovskite neodymium nickelate films on  $\text{SrTiO}_3(001)$ , *Phys. Rev. B* **102**, 020502(R) (2020).
- [55] R. Di Capua, M. Verma, M. Radović, N. C. Plumb, J. H. Dil, Z. Ristić, E. B. Guedes, G. M. De Luca, D. Preziosi, Z. Wang, A. P. Weber, R. Pentcheva, and M. Salluzzo, Two-dimensional electron gas at the (001) surface of ferromagnetic  $\text{EuTiO}_3$ , *Phys. Rev. Res.* **3**, L042038 (2021).
- [56] R. Pentcheva, M. Huijben, K. Otte, W. E. Pickett, J. E. Kleibeuker, J. Huijben, H. Boschker, D. Kockmann, W. Siemons, G. Koster, H. J. W. Zandvliet, G. Rijnders, D. H. A. Blank, H. Hilgenkamp, and A. Brinkman, Parallel Electron-Hole Bilayer Conductivity from Electronic Interface Reconstruction, *Phys. Rev. Lett.* **104**, 166804 (2010).

# DuEPublico

Duisburg-Essen Publications online

UNIVERSITÄT  
DUISBURG  
ESSEN

*Offen im Denken*

ub | universitäts  
bibliothek

This text is made available via DuEPublico, the institutional repository of the University of Duisburg-Essen. This version may eventually differ from another version distributed by a commercial publisher.

**DOI:** 10.1103/PhysRevResearch.5.013199

**URN:** urn:nbn:de:hbz:465-20230821-152055-2



This work may be used under a Creative Commons Attribution 4.0 License (CC BY 4.0).